

UC Berkeley

UC Berkeley Previously Published Works

Title

Detection of $z \sim 2.3$ Cosmic Voids from 3D Ly α Forest Tomography in the COSMOS Field

Permalink

<https://escholarship.org/uc/item/0d8705qv>

Journal

Astrophysical Journal, 861(1)

ISSN

0004-637X

Authors

Krolewski, A
Lee, KG
White, M
[et al.](#)

Publication Date

2018-07-01

DOI

10.3847/1538-4357/aac829

Peer reviewed



Detection of $z \sim 2.3$ Cosmic Voids from 3D Ly α Forest Tomography in the COSMOS Field

Alex Krolewski¹ , Khee-Gan Lee^{2,11} , Martin White^{1,2} , Joseph F. Hennawi³ , David J. Schlegel² , Peter E. Nugent^{1,2} , Zarija Lukić², Casey W. Stark⁴ , Anton M. Koekemoer⁵ , Olivier Le Fèvre⁶, Brian C. Lemaux^{6,7}, Christian Maier⁸ , R. Michael Rich⁹, Mara Salvato¹⁰ , and Lidia Tasca⁶

¹ Department of Astronomy, University of California at Berkeley, New Campbell Hall, Berkeley, CA 94720, USA; krolewski@berkeley.edu

² Lawrence Berkeley National Lab, 1 Cyclotron Road, Berkeley, CA 94720, USA

³ Department of Physics, Broida Hall, University of California at Santa Barbara, Santa Barbara, CA 93106, USA

⁴ Google Inc., 1600 Amphitheatre Parkway, Mountain View, CA 94043, USA

⁵ Space Telescope Science Institute, 3700 San Martin Drive, Baltimore, MD 21218, USA

⁶ Aix Marseille Université, CNRS, LAM (Laboratoire d'Astrophysique de Marseille) UMR 7326, F-13388, Marseille, France

⁷ Department of Physics, University of California, Davis, One Shields Ave., Davis, CA 95616, USA

⁸ University of Vienna, Department of Astrophysics, Tuerkenschanzstrasse 17, A-1180 Vienna, Austria

⁹ Department of Physics and Astronomy, University of California at Los Angeles, Los Angeles, CA 90095, USA

¹⁰ Max Planck Institute for Extraterrestrial Physics, Gießenbachstrae 1, D-85741 Garching bei München, Germany

Received 2017 October 16; revised 2018 May 23; accepted 2018 May 24; published 2018 July 3

Abstract

We present the most distant detection of cosmic voids ($z \sim 2.3$) and the first detection of three-dimensional voids in the Ly α forest. We used a 3D tomographic map of the absorption with an effective comoving spatial resolution of $2.5 h^{-1}$ Mpc and a volume of $3.15 \times 10^5 h^{-3}$ Mpc³, which was reconstructed from moderate-resolution Keck I/LRIS spectra of 240 background Lyman-break galaxies and quasars in a 0.16 deg^2 footprint in the COSMOS field. Voids were detected using a spherical overdensity finder calibrated from hydrodynamical simulations of the intergalactic medium (IGM). This allows us to identify voids in the IGM corresponding to voids in the underlying matter density field, yielding a consistent volume fraction of voids in both data (19.5%) and simulations (18.2%). We fit excursion set models to the void radius function and compare the radially averaged stacked profiles of large voids ($r > 5 h^{-1}$ Mpc) to stacked voids in mock observations and the simulated density field. Comparing with 432 coeval galaxies with spectroscopic redshifts in the same volume as the tomographic map, we find that the tomography-identified voids are underdense in galaxies by 5.95σ compared to random cells.

Key words: cosmology; observations – intergalactic medium – large-scale structure of universe – quasars; absorption lines

Supporting material: machine-readable table

1. Introduction

Cosmic voids offer a laboratory for studying cosmology and galaxy formation in extreme environments. Voids are large (Mpc to tens of Mpc), slightly prolate regions nearly devoid of galaxies, which constitute the majority of the universe's volume (van de Weygaert & Platen 2011). Voids are surrounded by the beaded, filamentary network of the cosmic web and expand and evacuate as matter streams onto filaments and collapses into halos (Bond et al. 1996). Matter streams outward most quickly in the center of voids, where the density is lowest, creating a so-called bucket profile with a uniform inner density ($\delta \sim -0.7$ – -0.9 ; Hamaus et al. 2014; Sutter et al. 2014a). The exact shape of the profile is dependent on both the void finder and the large-scale environment of the void under consideration: small voids are often subvoids within a large-scale overdensity and are surrounded by a ridge of higher density, while large voids (as well as voids found by spherical overdensity finders; see White & Padmanabhan 2017) typically have a smooth profile approaching the mean density from below (Hamaus et al. 2014; Cai et al. 2016). While isolated voids become more isotropic over time (Sheth & van de Weygaert 2004), voids in the real universe remain prolate due

to external tides and collisions with neighboring sheets and filaments (van de Weygaert & Platen 2011).

Voids are especially useful for studying components of the universe that cluster weakly, such as dark energy (Lee & Park 2009; Lavaux & Wandelt 2012) or massive neutrinos (Villaescusa-Navarro et al. 2013; Massara et al. 2015; Banerjee & Dalal 2016): since voids are underdense in the clustered components of the universe (dark matter and baryons), unclustered components will have a maximal effect on the dynamics within voids (Goldberg & Vogeley 2004). Voids are also sensitive probes of modified gravity theories, which may be screened in higher-density regions (Clampitt et al. 2013).

Prospects for void cosmology have been studied using several different observables. Since voids are spherical, on average, the Alcock–Paczynski test (Alcock & Paczynski 1979) can be performed on sufficiently large stacks of voids (Ryden 1995; Lavaux & Wandelt 2012). Other sensitive observables include void–galaxy cross-correlations and redshift-space distortions (Cai et al. 2016; Hamaus et al. 2017), the integrated Sachs–Wolfe effect from stacked voids (Granett et al. 2008; Cai et al. 2017; Kovács et al. 2017), weak lensing of stacked voids (Higuchi et al. 2013; Krause et al. 2013; Melchior et al. 2014; Barreira et al. 2015; Clampitt & Jain 2015; Gruen et al. 2016; Cai et al. 2017), void counts to probe modified gravity (Li et al. 2012; Clampitt et al. 2013; Cai et al. 2015;

¹¹ Hubble Fellow.

Lam et al. 2015; Zivick et al. 2015) or dark energy (Pisani et al. 2015; Pollina et al. 2016), and void ellipticities (Park & Lee 2007; Bos et al. 2012). Extending the study of cosmic voids to higher redshifts could allow for better constraints on redshift-dependent models, such as early dark energy (Doran & Robbers 2006).

Studying galaxies in voids can illuminate the influence of environment on galaxy evolution. It is shown by N -body simulations that the halo mass function abruptly changes from sheets to voids, leading to a dearth of dwarf galaxies in voids. This is the so-called “void phenomenon,” originally identified as a tension with Λ CDM by Peebles (2001) but explained in the context of the halo model by Tinker & Conroy (2009). Comparisons of void galaxies to galaxies in average environments suggest that the change in the stellar mass function plays a dominant role in modifying galaxy properties as compared to the field (Hoyle et al. 2005; Tinker et al. 2008; Alpaslan et al. 2015; Penny et al. 2015; Beygu et al. 2016), and void galaxies show a similar diversity in morphology to field galaxies of the same stellar mass (Beygu et al. 2017). Recently, some hints have emerged that void galaxies may have a slightly higher mass-to-light ratio than field galaxies of the same mass (Alpaslan et al. 2015), higher H I masses at low stellar mass (Beygu et al. 2016), and enhanced star formation rate-to-H I mass ratio (Kreckel et al. 2012), although these effects remain quite subtle. Since the global star formation rate of the universe is much higher at $z \sim 2$ than at $z \sim 0$, it would be interesting to study whether stellar mass remains the primary driver of void galaxy properties at $z \sim 2$ or whether environment begins to play a more significant role.

Observational studies of voids have been limited to low-to-moderate redshift, where sufficiently dense galaxy surveys are available to identify voids. Voids have been identified in 2dF (Ceccarelli et al. 2006), SDSS (Pan et al. 2012; Sutter et al. 2012), VIPERS (Micheletti et al. 2014), BOSS (Mao et al. 2017b), DES (Sánchez et al. 2017), and DEEP2 (Conroy et al. 2005). The SDSS and BOSS voids have also been used for cosmological analyses (Sutter et al. 2014c; Hamaus et al. 2016; Mao et al. 2017a). Finding voids with a radius of a few Mpc requires a large-volume galaxy survey with resolution of a few Mpc, which becomes increasingly difficult above $z \sim 1$ (Stark et al. 2015a).

At higher redshifts, Ly α forest tomography (Pichon et al. 2001; Caucci et al. 2008; Lee et al. 2014) offers an alternative method for obtaining large-volume, densely spaced surveys of the matter density field. Using spectroscopic observations of closely spaced quasars and Lyman-break galaxies, Ly α forest tomography can reconstruct the 3D intergalactic medium (IGM) absorption field with a resolution of a few Mpc and on cosmological volumes of $10^6 h^{-3} \text{Mpc}^3$ (Lee et al. 2014). This technique allows for recovery of the cosmic web with comparable fidelity to $z < 0.5$ galaxy surveys (Lee & White 2016; Krolewski et al. 2017), which requires considerably greater spatial resolution than $z \sim 2$ galaxy surveys can provide. At $z \sim 2.5$, absorption with optical depth unity arises from neutral hydrogen with three times the mean density; thus, the Ly α forest is ideal for probing underdense structures such as voids. Indeed, Stark et al. (2015a) found that a simple spherical overdensity void finder could recover $r \geq 6 h^{-1} \text{Mpc}$ voids in the IGM flux field at 60% fidelity, allowing detection of ~ 100 such voids in a 1 deg^2 survey.

In this paper, we make the first detection of $z \sim 2$ cosmic voids in the 3D Ly α forest using the COSMOS Ly α Mapping and Tomography Observations (CLAMATO) survey (Lee et al. 2017). CLAMATO is the first survey to systematically use Lyman-break galaxies for Ly α forest analysis. It has produced a 3D map of the IGM absorption field with resolution $2.5 h^{-1} \text{Mpc}$ and volume $3.15 \times 10^5 h^{-3} \text{Mpc}^3$, using Keck I/LRIS observations of the central 0.16 deg^2 of the COSMOS field.

While we are not the first to consider voids in the IGM, this work is distinct from previous observational efforts: Tejos et al. (2012) worked at $z \sim 0$; Rollinde et al. (2003) used only four sight lines, leading to large uncertainties; and Viel et al. (2008) were limited to analyzing flux in 1D skewers.

The detection of $z \sim 2$ voids extends observational studies of voids to a much higher redshift range. In the future, high-redshift voids could allow for studies of the redshift evolution of void galaxies and properties over a much larger redshift baseline and better constraints on redshift-dependent dark energy and modified gravity models.

We begin by describing the data (Section 2) and simulations (Section 3) used in this paper. Next, we determine appropriate spherical overdensity thresholds by matching the void fraction in mock tomographic observations to the fraction of true voids in the density field (Section 4.1). We apply these thresholds to data in Section 4.2. In Section 5, we compare the tomography-identified voids to the positions of coeval galaxies with spectroscopic redshifts and find that the voids are $\sim 6\sigma$ underdense in coeval galaxies. We discuss the properties of the voids in Section 6 (including the void radius function and stacked void profile) and present our conclusions in Section 7.

In this paper, we use a flat Λ CDM cosmology with $\Omega_m = 0.31$ and $h = 0.7$. While the simulations use a slightly different cosmology (see Section 3), the differences are small enough that the discrepancy will have a negligible impact on the results presented here.

2. Data

We identify voids in the reconstructed IGM tomographic map from the first data release of the CLAMATO survey.¹² The observations are described in detail by Lee et al. (2017), but we briefly summarize the pertinent details here.

The survey targeted $2.3 < z < 3$ background Lyman-break galaxies and quasars with the LRIS spectrograph (Oke et al. 1995; Steidel et al. 2004) on the Keck I telescope at Maunakea, Hawai’i, to measure the foreground Ly α forest absorption. This program targeted the COSMOS field to take advantage of rich existing data sets and achieve a high targeting efficiency. We observed 23 slit masks (18 regular slit masks and 5 “special” slit masks designed to fill in gaps in coverage) with ~ 20 targets per mask. We successfully reduced 437 galaxies and active galactic nuclei (AGNs), of which 289 had high-confidence redshifts and 240 were usable for the Ly α forest analysis at our targeted absorption redshift range of $2.05 < z < 2.55$. The primary criterion for the selection of the background spectra was the signal-to-noise ratio on the continuum in the Ly α forest (i.e., ratio of estimated continuum to pixel noise; hereafter we refer to this quantity as S/N): we required $S/N \geq 1.2 \text{ pixel}^{-1}$.

¹² We use CLAMATO v4, available at doi:10.5281/zenodo.1292459.

The intrinsic continua of the background sources were estimated using mean-flux regulation (Lee et al. 2012, 2013), which adjusts the mean Ly α forest transmission within each sight line to be consistent with $\langle F(z) \rangle$ estimates from the literature; we used Faucher-Giguère et al. (2008). Based on Lee et al. (2012), we estimate that the continuum errors are approximately $\sim 10\%$ rms for the noisiest spectra ($S/N \sim 2 \text{ pixel}^{-1}$) and improve to $\sim 4\%$ rms for $S/N \sim 10$ spectra.

From the observed flux density and the fitted continuum, we compute the Ly α forest fluctuations, δ_F ,

$$\delta_F = \frac{f}{C \langle F(z) \rangle} - 1, \quad (1)$$

where $\langle F(z) \rangle$ is the mean Ly α transmission from Faucher-Giguère et al. (2008; the power-law fit from Table 5, including metals, with bins of width $\Delta z = 0.1$).

We use these values of δ_F as input for the Wiener filter tomographic reconstruction. To avoid a flared map geometry, we use a constant conversion between redshift and comoving distance, $d\chi/dz$, and a constant transverse comoving distance χ , both evaluated at $z = 2.3$. With a fixed angular footprint on the sky, this amounts to an $\sim 20\%$ change in the reconstruction kernel size over the length of the map. While our mocks lack this redshift-dependent reconstruction kernel, we find that our results are virtually unchanged when we use an evolving $\chi(z)$ and $d\chi/dz(z)$. Specifically, the volume fraction of voids drops from 19.5% to 19.2% (0.2σ), the voids remain $\sim 6\sigma$ underdense in coeval galaxies, and the void radius function and profile change by $< 1\sigma$ at all bins. Thus, we keep the simpler redshift- and angle-distance conversions presented above but caution that future, more detailed analysis will likely require more accurate coordinate conversions and thus a more complex map geometry.

We define an output grid with cells of comoving size $0.5 h^{-1} \text{ Mpc}$, transverse dimensions $30 \times 24 h^{-1} \text{ Mpc}$, and line-of-sight length $438 h^{-1} \text{ Mpc}$, corresponding to $2.05 < z < 2.55$. Thus, the total comoving volume is $3.15 \times 10^5 h^{-3} \text{ Mpc}^3$ over a survey geometry that is elongated along the line-of-sight (redshift) dimension but considerably smaller across the transverse dimensions. The effective sight-line spacing varies along the line of sight from $2.22 h^{-1} \text{ Mpc}$ at $z = 2.25$ to $3.15 h^{-1} \text{ Mpc}$ at $z = 2.45$.

We use a Wiener filtering algorithm developed by Stark et al. (2015b) to reconstruct the 3D IGM absorption field,

$$\delta_F^{\text{rec}} = \mathbf{C}_{\text{MD}} \cdot (\mathbf{C}_{\text{DD}} + \mathbf{N})^{-1} \cdot \delta_F, \quad (2)$$

where \mathbf{N} is the noise covariance, \mathbf{C}_{DD} is the data–data covariance, and \mathbf{C}_{MD} is the map–data covariance. We assume that the noise covariance is diagonal, with $N_{ij} = n_i^2 \delta_{ij}$, where n_i is the pixel noise. To avoid weighting any sight lines too heavily, we set a minimum noise level of 0.2. We further assume that $\mathbf{C}_{\text{MD}} = \mathbf{C}_{\text{DD}} = \mathbf{C}$:

$$\mathbf{C} = \sigma_F^2 \exp \left[-\frac{\Delta x_{\perp}^2}{2l_{\perp}^2} - \frac{\Delta x_{\parallel}^2}{2l_{\parallel}^2} \right]. \quad (3)$$

We use $\sigma_F^2 = 0.05$, $l_{\perp} = \langle d_{\perp} \rangle = 2.5 h^{-1} \text{ Mpc}$, and $l_{\parallel} = 2.0 h^{-1} \text{ Mpc}$. While in previous works, we have additionally Gaussian-smoothed the output tomographic reconstruction, in this paper, we apply no additional smoothing to the map, following Stark et al. (2015a).

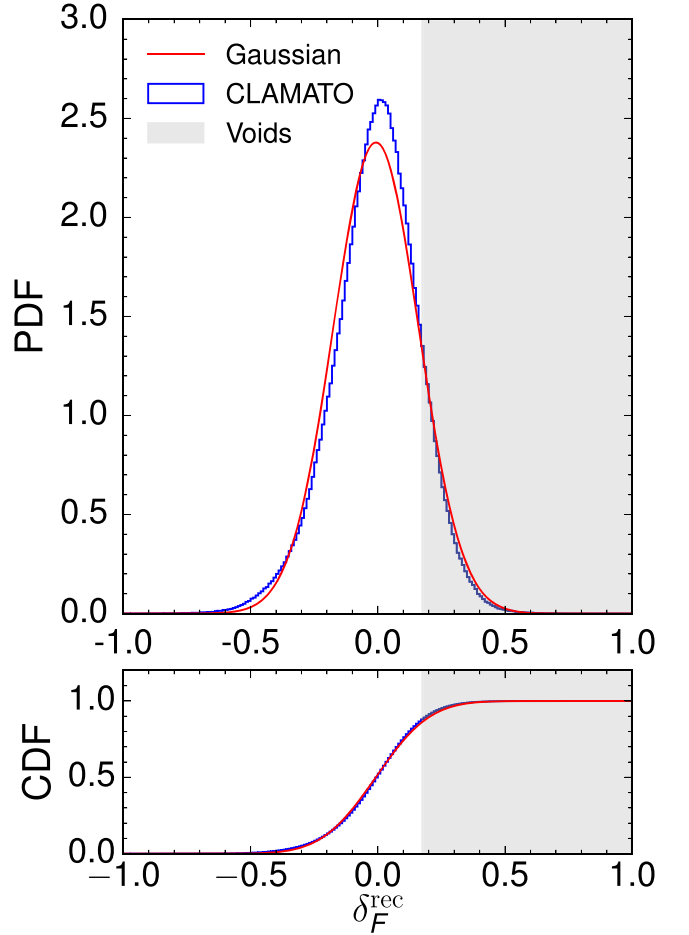


Figure 1. Probability density and cumulative distributions of δ_F^{rec} in the CLAMATO map compared to a Gaussian. The lower edge of the gray shaded region is the threshold for the average void density, $\delta_F^{\text{rec}} = 0.175$.

Hereafter, we identify voids in the Wiener-filtered map rather than in the pixel-level data. While it should be possible to develop a void finder that can be applied directly to the pixel-level data (a method that could, in principle, also be extended to the sparsely and irregularly sampled galaxy field), we leave the development of this method to future work.

Figure 1 shows the distribution of δ_F^{rec} in the Wiener-filtered map and overplots a Gaussian distribution with the same mean and standard deviation. Although the distribution of δ_F^{rec} is reasonably well approximated by a Gaussian, particularly in the high δ_F^{rec} region where the voids lie, the underlying density field smoothed on scales of $2.5 h^{-1} \text{ Mpc}$ is quite non-Gaussian, indicating that there is cosmological information in the presence and distribution of voids beyond the two-point statistics in the map.

3. Simulations

We use mock tomographic reconstructions from Ly α forest simulations to both calibrate the thresholds for the spherical overdensity void finder and understand the effects of survey geometry and sample variance on our results. We use both hydrodynamic simulations of the IGM and N -body simulations of the density field with the Ly α forest modeled using the fluctuating Gunn–Peterson approximation. Each simulation has its advantages and disadvantages: the hydrodynamic simulation more accurately models the physics of the IGM but is

hampered by a relatively small volume of $(100 h^{-1} \text{ Mpc})^3$; the larger $(256 h^{-1} \text{ Mpc})^3$ N -body simulation enables us to create many realizations of CLAMATO-like volumes with approximately the correct survey geometry (though considerably shorter along the line of sight), but its IGM prescription is only approximate. Throughout this paper, we use both simulations and, wherever possible, we endeavor to compare the N -body and hydrodynamic simulation results to ensure robustness to different simulation methods and included physics.

3.1. Hydrodynamical Simulations

The hydrodynamic simulations of the IGM are generated with the N -body+plus+Eulerian hydrodynamics Nyx code (Almgren et al. 2013). It has a $100 h^{-1} \text{ Mpc}$ box size with 4096^3 cells and particles, resulting in a dark matter particle mass of $1.02 \times 10^6 h^{-1} M_\odot$ and spatial resolution of $24 h^{-1} \text{ kpc}$. As discussed in Lukić et al. (2015), this resolution is sufficient to resolve the filtering scale below which the IGM is pressure supported and to reproduce the $z = 2.4$ flux statistics to a percent accuracy within the range of physics included (we neglect radiative transfer and do not model high column density systems well). We use a snapshot at $z = 2.4$. This simulation uses a flat Λ CDM cosmology with $\Omega_m = 0.3$, $\Omega_b = 0.047$, $h = 0.685$, $n_s = 0.965$, and $\sigma_8 = 0.8$, consistent with the latest Planck measurements (Planck Collaboration et al. 2016). It uses the ionizing background prescription of Haardt & Madau (1996), producing an IGM temperature-density relationship with $T_0 \sim 10^4 \text{ K}$ and $\gamma \sim 1.55$ at $z = 2$. This simulation does not model star formation and hence has no feedback from stars, galaxies, or AGNs, but these are expected to have a negligible effect on the Ly α forest statistics (Viel et al. 2013).

We generate 512^2 absorption skewers with a spacing of $0.2 h^{-1} \text{ Mpc}$ and sample from these skewers to create mock data. We compute the Ly α forest flux fluctuation along each skewer, then shift to redshift space and Doppler broaden the skewers using the gas temperature. The HI optical depths, τ , in the mock spectra are adjusted to match the mean flux from Faucher-Giguère et al. (2008) at $z = 2.3$ ($\langle F \rangle = 0.8189$); we use a single mean flux throughout the entire line-of-sight direction, since neither simulation box is as long as the line-of-sight length of the map. Absorption skewers are randomly selected with mean sight-line spacing $\langle d_\perp \rangle = 2.5 h^{-1} \text{ Mpc}$ and rebinned along the line of sight with resolution $0.84 h^{-1} \text{ Mpc}$, corresponding to the 1.2 \AA LRIS pixels. Using a single sight-line spacing is approximate, as the mean transverse separation of CLAMATO sight lines varies with redshift (Lee et al. 2017); our choice of $\langle d_\perp \rangle = 2.5 h^{-1} \text{ Mpc}$ is slightly conservative compared to the CLAMATO $\langle d_\perp \rangle = 2.37 h^{-1} \text{ Mpc}$. This difference should not be significant, since we use the same correlation lengths for the tomographic reconstructions (l_\perp and l_\parallel in Equation (3)) in both mocks and data. Finally, the skewers are smoothed with a Gaussian kernel with $2.8 h^{-1} \text{ Mpc}$ FWHM ($\sim 4 \text{ \AA}$) to account for the spectral resolution of LRIS at 4000 \AA .

We add both random noise and correlated continuum error to each skewer. Random noise is simulated assuming the S/N per pixel is a unique constant for each skewer. To determine the S/N for each skewer, we draw from a power-law S/N distribution $dn_{\text{los}}/dS/N \propto S/N^{-\alpha}$ (Stark et al. 2015b, hereafter S15b), where S/N ranges between 1.4 and infinity. From S15b,

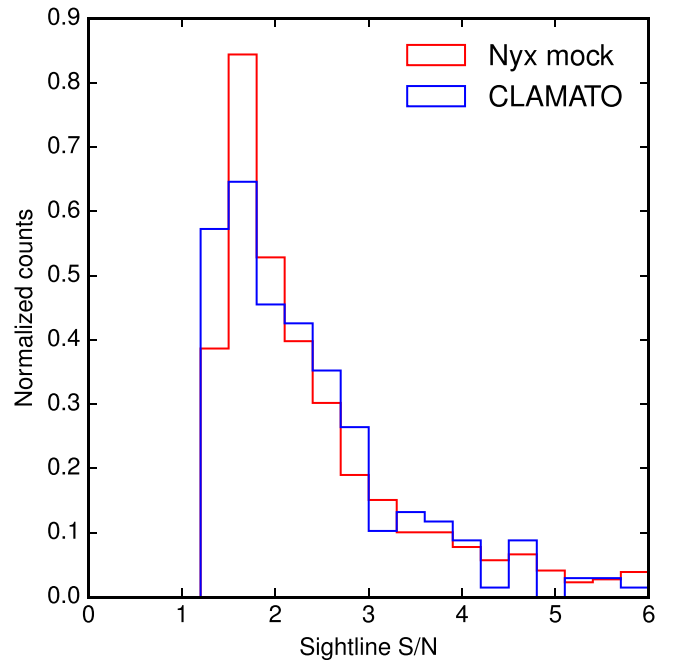


Figure 2. Distribution of S/N per pixel for CLAMATO sight lines and Nyx mock sight lines.

we use $\alpha = 2.7$ for the $\langle d_\perp \rangle = 2.5 h^{-1} \text{ Mpc}$ reconstructions. The minimum S/N of 1.4 in the mock sight lines is slightly higher than the minimum S/N of 1.2 in CLAMATO; the S/N distribution in CLAMATO rolls over below an S/N of 1.5, perhaps owing to the difficulty of determining redshifts for low-S/N galaxies. Therefore, a minimum S/N of 1.4 provides the best match to the CLAMATO S/N distribution, with a median S/N of 2.1 in CLAMATO and 2.15 in the mock sight lines (Figure 2). We then use the S/N for each sight line to determine the pixel noise n (i.e., the error on δ_F):

$$n = \frac{1}{S/N \langle F \rangle}. \quad (4)$$

Subsequently, we add a random Gaussian deviate with standard deviation n to the δ_F values in each pixel and use the resulting noisy δ_F and n as input to the Wiener filter (Equation (2)).

We also model the continuum-fitting error,

$$F_{\text{obs}} = \frac{F_{\text{sim}}}{1 + \delta_{\text{cont}}}, \quad (5)$$

where δ_{cont} is a random Gaussian deviate, identical for all pixels within a skewer, with mean zero and standard deviation σ_{cont} . Following Lee et al. (2012), σ_{cont} is a function of the S/N, with lower S/N spectra having higher continuum error and vice versa. We fit a function to the data points in Figure 8 of Lee et al. (2012) for $z = 2.35$,

$$\sigma_{\text{cont}} = \frac{a}{S/N} + b, \quad (6)$$

where $a = 0.2054$ is a free parameter fit to the data and $b = 0.015$ is the rms fitting error in the absence of continuum structure and noise, to which the continuum error should asymptote in the case of infinite S/N. To be conservative, we cap the continuum error for $S/N > 10$ at 4%.

We apply the same Wiener filter interpolation to the mock sight lines as to our data, with the same noise floor of 0.2 as in the data. Just as in the data reconstruction, we use pixels $0.5 h^{-1} \text{Mpc}$ on a side.

3.2. Large-volume N -body Simulations

The hydrodynamical simulation is too small ($L = 100 h^{-1} \text{Mpc}$) to mimic the elongated CLAMATO survey geometry. To better understand the effect of survey geometry and sample variance on our results, we therefore also use a larger N -body simulation (White et al. 2010). This is a publicly available simulation used in our previous papers (Lee et al. 2015; Stark et al. 2015a, 2015b), so we describe it only briefly here.

The N -body simulation uses 2560^3 particles of $8.6 \times 10^7 h^{-1} M_\odot$ in a $256 h^{-1} \text{Mpc}$ periodic box. The cosmological parameters are $\Omega_m = 0.31$, $\Omega_b h^2 = 0.022$, $h = 0.677$, $n_s = 0.9611$, and $\sigma_8 = 0.83$, and initial conditions are generated using second-order Lagrangian perturbation theory at $z_{ic} = 150$. The particles were evolved forward using the TreePM code of White (2002), and we use output at $z = 2.5$. The Ly α absorption field was generated with the fluctuating Gunn–Peterson approximation assuming a pressure-filtering scale of $100 h^{-1} \text{kpc}$ and a power-law temperature–density relationship with $T_0 = 2 \times 10^4 \text{K}$ and $\gamma = 1.6$.

Taking advantage of the larger volume of the N -body box, we create both a single mock reconstruction spanning the entire 256^3 box and 64 reconstructed subvolumes, each with dimensions $32 \times 32 \times 256$, which roughly match the CLAMATO survey geometry and volume. The exact CLAMATO survey geometry ($30 \times 24 \times 438 h^{-1} \text{Mpc}$) cannot be reproduced even with the $256 h^{-1} \text{Mpc}$ simulation, but it provides at least a rough comparison.

We generated skewers using 640^3 grids of the Ly α absorption field. We followed exactly the same procedures to generate mock CLAMATO observations from the N -body simulations as from the hydrodynamic simulations.

4. Void Finding

4.1. Calibrating the Void Finder

To identify cosmic voids in the IGM map, we use the void-finding procedure described in Stark et al. (2015a), which is analogous to the spherical overdensity techniques used for halo-finding in N -body simulations but applied to underdensities. While this method cannot fully capture the complex and anisotropic shapes of voids, it is simple, easy to use, and easy to apply to both the density field and flux field. While alternative finders (i.e., watershed methods; Neyrinck 2008) are widely used in the literature, the complexity of these void finders may lead to poor performance in the presence of noise in the tomographic maps (e.g., Stark et al. 2015a). Moreover, as this is the first attempt at void detection in a qualitatively new data set, the spherical overdensity finder has an attractive simplicity.

To identify voids, we begin by finding all points with δ_F greater than some threshold¹³ or density lower than a separate threshold (“SO threshold”). Spheres are grown around all these points until the average δ_F (density) in the sphere reaches a second threshold (“SO average”). All spheres with

¹³ Recall that δ_F has a negative sign convention with respect to overdensities.

Table 1
Volume Fraction for Different Void Thresholds in Simulated Catalogs

Field	SO Thresh.	SO Average	Vol. Frac.
ρ	$0.2\bar{\rho}$	$0.4\bar{\rho}$	0.180
ρ_{red}	$0.15\bar{\rho}$	$0.3\bar{\rho}$	0.173
δ_F	0.192	0.152	0.180
δ_F^{rec}	0.220	0.175	0.180
$\delta_F^{\text{rec}} (N\text{-body})$	0.220	0.175	0.182
CLAMATO	0.220	0.175	0.195

Note. Comparison of volume fraction of voids in data and simulations ($100 h^{-1} \text{Mpc}$ hydrodynamic box and $256 h^{-1} \text{Mpc}$ N -body box). All simulated fields are from the hydrodynamic box unless otherwise noted. The simulated fields include real and redshift-space density fields, the underlying flux δ_F , and the reconstructed flux δ_F^{rec} , with CLAMATO-like sight-line spacing and realistic noise and continuum error. Both δ_F and δ_F^{rec} are adjusted to the mean flux used in CLAMATO at $z = 2.3$.

$r \leq 2 h^{-1} \text{Mpc}$ are removed, and overlapping voids are eliminated by only keeping the void with the largest radius.

The SO threshold and SO average chosen in this paper are motivated by the values given in Table 1 of Stark et al. (2015a). However, these thresholds are inapplicable to CLAMATO because they neglect continuum error in the mock sight lines and do not match the mean flux of the observations. Continuum error is particularly important at the high-transmission (high δ_F) end (Lee et al. 2015). By combining Equations (1) and (5) and Taylor expanding in the small quantity δ_{cont} , the change in δ_F due to continuum error is $\delta_{\text{cont}} F / \langle F \rangle$; thus, continuum error is more important at the high-flux end than the low-flux end. Moreover, since continuum error is correlated along a sight line, it will both create spurious voids and erase real voids. Since continuum error increases the spread of δ_F^{rec} at the high-flux end, adding continuum error will lead to more points with extreme values of δ_F^{rec} and thus increase the void fraction.

Following Stark et al. (2015a), we begin by finding voids in the real and redshift-space density fields. We use the same real-space thresholds as Stark et al. (2015a), with an SO threshold of $\rho = 0.2\bar{\rho}$ and SO average of $\rho = 0.4\bar{\rho}$. The SO threshold is derived from the central density of a void at shell crossing in the spherical top-hat collapse model (van de Weygaert & Platen 2011); the SO average is less well motivated and was chosen by Stark et al. (2015a) to best create visually identified voids surrounded by edges (i.e., the bucket profile). The values of the SO threshold and average in the redshift-space density are arbitrary; we use the same values as Stark et al. (2015a), $\rho_{\text{red}} = 0.15\bar{\rho}$ for the SO threshold and $\rho_{\text{red}} = 0.3\bar{\rho}$ for the SO average. We expect the thresholds to be lower in redshift space than in real space due to outflows from voids.

We find similar volume fractions in the N -body and hydrodynamic simulations for voids in the real-space and redshift-space density fields (17%–18% in hydrodynamic simulations in Table 1 compared to 15% in N -body from Table 1 in Stark et al. 2015a). The small remaining discrepancies may arise from the slightly different cosmologies of the two simulations and the fact that the N -body simulations neglect baryonic effects.

We choose the SO thresholds in the underlying flux field δ_F and the mock CLAMATO reconstruction δ_F^{rec} to match the void fraction in the redshift-space density field. These thresholds are listed in Table 1. We do not use the same thresholds for δ_F as

Stark et al. (2015a), since we rescale $\langle F \rangle$ to $\langle F(z = 2.3) \rangle$ from Faucher-Giguère et al. (2008), changing the range of δ_F and necessitating the use of a different threshold. This allows us to apply the same SO thresholds to both the observations and the two simulations. Furthermore, unlike Stark et al. (2015a), we do not use the same SO thresholds for δ_F and δ_F^{rec} , since the presence of continuum error substantially broadens the probability distribution function (PDF) of δ_F^{rec} , yielding a 24% void fraction in δ_F^{rec} versus 18% void fraction in δ_F for the same SO thresholds. Due to the sensitivity of the void fraction to both the mean flux and the continuum error, we emphasize that picking appropriate thresholds requires realistic mock reconstructions. As a result, these thresholds are only applicable to the data presented in this paper.

In the presence of continuum error, void recovery is slightly poorer than reported in Stark et al. (2015a). As in Stark et al. (2015a), we characterize the fidelity of void recovery using the volume overlap fraction and match error between the redshift-space density field and mock-reconstruction voids. The volume overlap fraction is defined as the fraction of the volume of voids in one catalog that overlaps voids in another catalog, while the match error is defined for each pair of voids A and B:

$$\epsilon = \frac{\sqrt{(r_A - r_B)^2 + |\mathbf{x}_A - \mathbf{x}_B|^2/3^2}}{r_A}. \quad (7)$$

For each void in catalog A, the match error is the minimum of the match error with all voids in catalog B. Following Stark et al. (2015a), two voids are defined as well matched if $\epsilon < 0.3$; thus, the match fraction is the fraction of all voids in a catalog with $\epsilon < 0.3$.

Depending on the comparison sample, these quantities can describe either the purity or the completeness of the void catalog: the completeness is characterized by the (overlap or match) fraction of density voids that are also found in the reconstruction, while the purity is characterized by the fraction of voids in the reconstruction that also exist in the density field. We find that the completeness and purity drop 5–10 points compared to an identical mock observation without continuum error. Overall, we amend the conclusion of Stark et al. (2015a) that 60% of $r \geq 5 h^{-1} \text{Mpc}$ voids are recovered by CLAMATO-like IGM tomography, instead finding the recovery of these large voids to be closer to 40%–45%.

In Figure 3, we plot the completeness and purity of the volume overlap fraction and match fraction compared between voids in mock IGM tomography and the redshift-space density field in the Nyx simulation as a function of void radius. For large voids, the completeness and purity of the match fraction and volume overlap fraction range between 30% and 45% for $r \sim 6 h^{-1} \text{Mpc}$. For small voids, the match fraction drops rapidly to $\sim 5\%$ for $r \sim 2 h^{-1} \text{Mpc}$, while the volume overlap fraction drops more slowly, to 35% for $r \sim 2 h^{-1} \text{Mpc}$. The same behavior was seen in Stark et al. (2015a) and reflects the fact that small voids may have poor centering and radius estimates due to tomographic noise artificially splitting or joining voids, but the volume overlap fraction may nevertheless remain substantial. We present Figure 3 as a guide for using the void catalog (Table 2). In Section 6, we only use the high-quality $r \geq 5 h^{-1} \text{Mpc}$ sample for studying void profiles, as this sample is less contaminated by noise in the tomographic reconstruction.

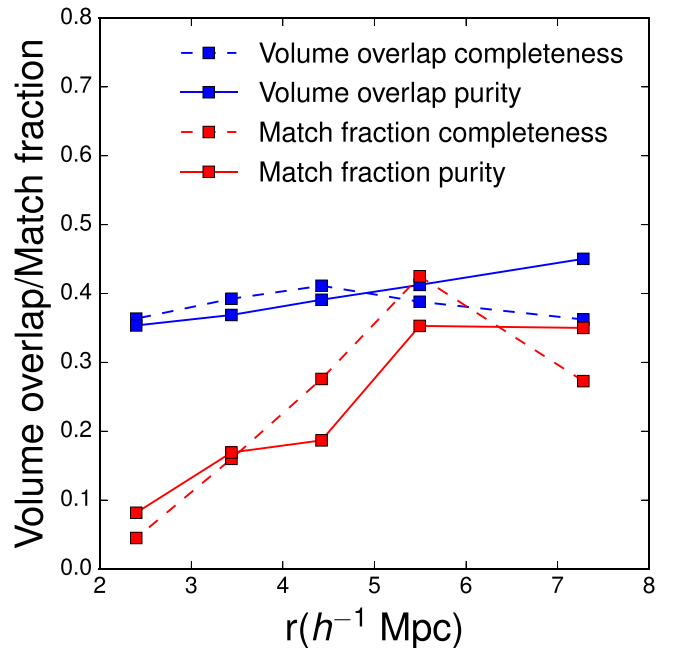


Figure 3. Purity and completeness of the volume overlap fraction and match fraction (fraction of voids with $\epsilon < 0.3$; see Equation (7)) as a function of void radius, measured between voids in the mock CLAMATO-like reconstructions and the redshift-space density field in the Nyx simulation.

Table 2
Voids in CLAMATO 2017 Map

Tomographic Map Position ($h^{-1} \text{Mpc}$)			Void Radius ($h^{-1} \text{Mpc}$)	Sky Position		
x	y	z		α (J2000)	δ (J2000)	Redshift
1.0	0.0	244.5	9.40	149.96480	2.15000	2.33
15.5	0.0	179.5	9.10	150.17943	2.15000	2.26
0.0	23.0	273.5	7.90	149.95000	2.49016	2.36
0.0	14.5	233.5	7.70	149.95000	2.36445	2.32
29.5	11.0	186.0	7.65	150.38665	2.31268	2.26
23.0	0.0	366.0	7.45	150.29044	2.15000	2.47
29.5	12.5	323.0	7.40	150.38665	2.33487	2.42
0.0	10.5	264.5	7.25	149.95000	2.30529	2.35
29.5	1.0	171.0	7.00	150.38665	2.16479	2.25
3.5	0.0	293.0	6.95	150.00181	2.15000	2.39

(This table is available in its entirety in machine-readable form.)

4.2. Application to Data

Applying the SO void finder to the 2017 CLAMATO IGM tomography map (Lee et al. 2017), we identify 355 $r > 2 h^{-1} \text{Mpc}$ cosmic voids, including 48 higher-quality $r \geq 5 h^{-1} \text{Mpc}$ voids, which we use for studying the void profile (Section 6). These voids fill 19.5% of the tomographic volume. Table 2 presents the radii and positions of the voids in both sky coordinates and tomographic map coordinates. In Figure 4, we overplot the voids and positions of coeval spectroscopic galaxies from MOSDEF, VUDS, zCOSMOS, and our own survey (see Section 5 for descriptions of these surveys). The figure shows slices through the volume, sampled every $2 h^{-1} \text{Mpc}$ in the right ascension or longitudinal direction. While most voids span more than one slice in this plot, for clarity, we only show voids in the slice where their

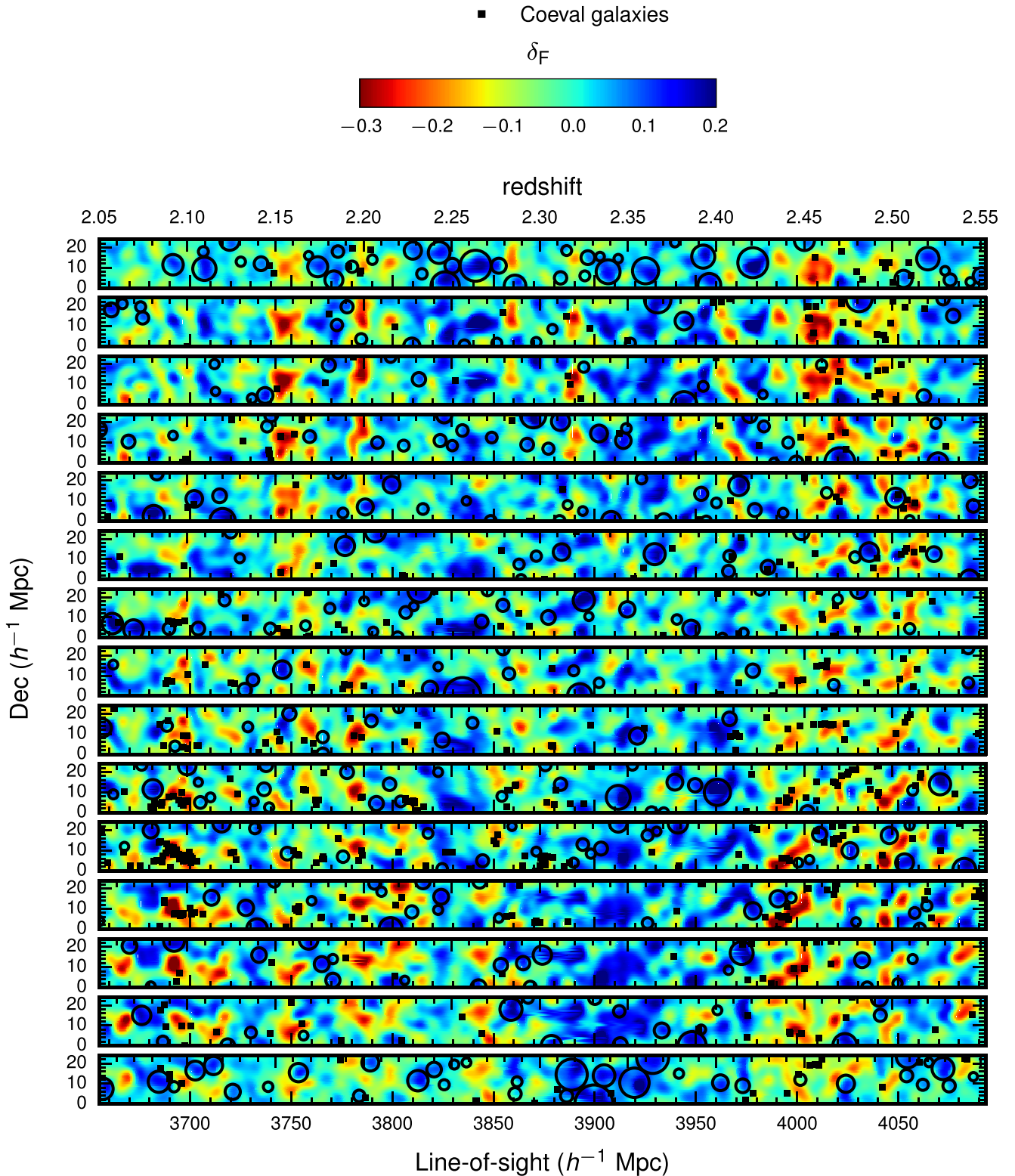


Figure 4. Voids (circles) and spectroscopic galaxies (squares) in the 2017 CLAMATO map. Blue indicates regions of low absorption and thus low density and high δ_F , while red indicates regions of high absorption, high density, and low δ_F . Each strip is a slice through the R.A. direction, spaced by $2 h^{-1}$ Mpc (strips are centered at R.A. = $1 h^{-1}$ Mpc, $3 h^{-1}$ Mpc, etc.). R.A. increases from the bottom strip to the top strip, and decl. increases from bottom to top on each strip. In each strip, we plot voids between 0 and $2 h^{-1}$ Mpc, 2 and $4 h^{-1}$ Mpc, etc. Note that we only plot voids on the strip where they are centered, although they may span multiple strips.

respective centers are located. Voids in Figure 4 appear largely devoid of galaxies, though a visual evaluation of the galaxy distribution is difficult owing to the very nonuniform selection function of the coeval galaxy spectroscopy. A quantitative

analysis of galaxies within the tomography-identified voids is presented in Section 5.

Figure 5 shows projections onto the plane of the sky for the four largest voids in our volume. In each projection, δ_F^{rec} is

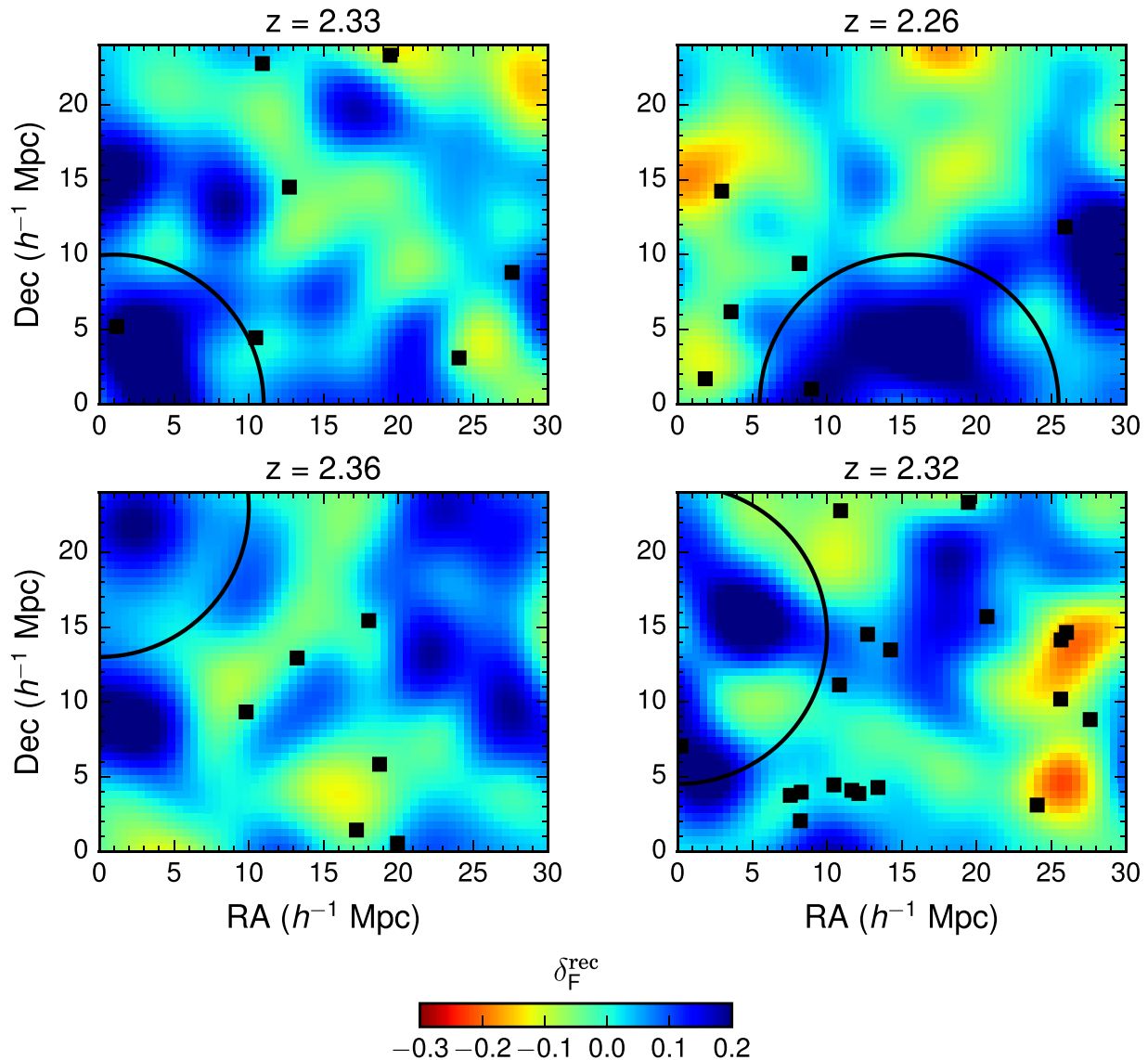


Figure 5. Projections of δ_F^{rec} onto the line of sight for the four largest voids in Table 2. In each panel, we plot the mean δ_F^{rec} averaged along a $20 h^{-1}$ Mpc length along the line of sight, centered at the redshift of each void. The black circle shows the void, and the black squares are coeval galaxies within $\pm 10 h^{-1}$ Mpc of the void center.

averaged across $20 h^{-1}$ Mpc along the line of sight (roughly the diameter of these voids). We show all coeval galaxies within this slice; therefore, galaxies with a different redshift from the void center may appear to lie in a void in Figure 5 while actually lying outside the void boundaries.

We highlight a complex of several voids between R.A. 0 and $10 h^{-1}$ Mpc, decl. 0 and $20 h^{-1}$ Mpc, and $z = 2.32$ – 2.37 . While this structure is broken into many voids by the spherical void finder, it is likely that these voids are part of a single structure spanning 10 – $20 h^{-1}$ Mpc, including the largest single void in the map, located at $(x, y, z) = (1, 0, 244.5) h^{-1}$ Mpc with radius $9.40 h^{-1}$ Mpc. As this void is located at the very bottom of the map, future observations extending the map will better probe this structure.

While the void fraction in CLAMATO (19.5%) is slightly higher than the void fraction in the mocks (18%), this difference can be entirely explained by sample variance. To quantify the impact of sample variance on the void fraction, we compute the void fraction in 64 subvolumes from our $256 h^{-1}$ Mpc N -body simulation. We find that the void

fractions in the subvolumes range from 14.5% to 22.8%, with a mean of 17.9% and a standard deviation of 1.8% (Figure 6). The small difference between the mean void fraction of this sample and the void fraction of the full N -body box (18.2%) is attributable to the effects of an elongated geometry on the N -body subvolumes and suggests that further deviation from the mean void fraction of the subvolumes due to the difference in survey geometry between CLAMATO and the N -body subvolumes is negligible. The void fraction in the CLAMATO map is thus $\sim 1\sigma$ higher than the void fraction in the N -body and hydrodynamic mocks.

In principle, matching the void fraction and void statistics in the simulation requires matching Ly α statistics such as the flux PDF and the flux power spectrum. In practice, matching the flux PDF especially is notoriously difficult, creating an additional source of systematic error that may lead to disagreement between void-finding in data and simulations. Moreover, discrepancies between theory and data are especially significant at the high-transmission end of the PDF, $F > 0.8$, where the voids lie (Bolton et al. 2017). The high-transmission

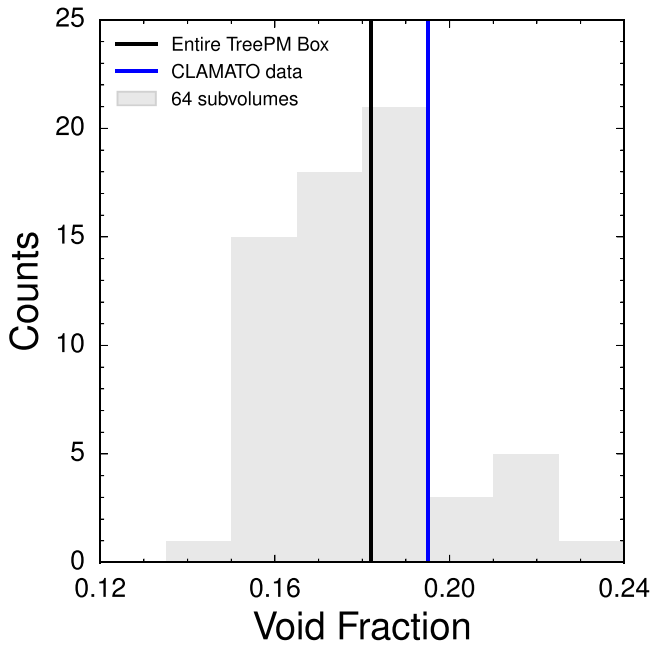


Figure 6. Volume fraction of cosmic voids from 64 subvolumes each with dimensions $32 \times 32 \times 256 h^{-1}$ Mpc (gray histogram), extracted from the N -body $256 h^{-1}$ Mpc simulation box, compared to the void fraction from the entire box (black line) and in CLAMATO data (blue line).

end of the flux PDF is particularly sensitive to the slope of the temperature–density relationship γ (White et al. 2010). Early measurements of the flux PDF suggested that $\gamma \lesssim 1$ (Bolton et al. 2008), in contrast to $\gamma \sim 1.6$ used in simulations here, though Lee (2012) pointed out that the effects of continuum error can be degenerate with changing γ . Later measurements of the flux PDF from BOSS with better-controlled continuum fitting found $\gamma \sim 1.6$ (Lee et al. 2015), though Rorai et al. (2017) claimed that even with improved continuum fitting, high-resolution quasar spectra still favor $\gamma \lesssim 1$, especially in underdense regions. Overall, Lee et al. (2015) showed that careful modeling of noise and systematic errors is critical for interpreting the flux PDF of low-resolution, noisy data such as that of BOSS or CLAMATO, with spectral resolution, pixel noise, and continuum error playing a particularly prominent role. They also found that additional discrepancies remained at high flux, which they solved by varying $\langle F \rangle$. Therefore, we carefully model pixel noise, continuum error, and Gaussian smoothing from the LRIS spectrograph. While we believe our current mocks are sufficiently realistic for an initial void detection and characterization, more careful mocks will be required for future cosmological analyses of IGM cosmic voids.

5. Void–galaxy Counts in Cells

The cosmic voids in the CLAMATO volume are by far the most distant sample of cosmic voids known at the present time. In comparison with the most distant $z \sim 1$ voids previously detected in galaxy redshift surveys (e.g., Conroy et al. 2005; Micheletti et al. 2014), our voids at $z \sim 2.3$ are $\sim 1.7 \times$ further in terms of comoving distance. Moreover, since CLAMATO achieves $\gtrsim 3$ times better density field resolution than existing or upcoming galaxy surveys at $z \sim 2$, it represents the best method for detecting high- z voids for the immediate future

(although all-sky interferometric 21 cm surveys may be able to detect voids at $z \sim 1$ –2; White & Padmanabhan 2017).

We validate the void-finding technique by counting coeval spectroscopic galaxies within the tomography-identified voids and comparing these counts to the number of galaxies within random cells with the same radius distribution and volume fraction. Exploiting the rich set of spectroscopic data that already exists within the COSMOS field, we use 110, 109, 118, and 95 galaxies from the VUDS (Le Fèvre et al. 2015), MOSDEF¹⁴ (Kriek et al. 2015), CLAMATO, and zCOSMOS-Deep (Lilly et al. 2007) surveys, respectively, which directly overlap with the CLAMATO map volume at $2.05 < z < 2.55$. By CLAMATO, we mean galaxies that were spectroscopically confirmed by CLAMATO to lie inside the map volume, e.g., sight lines for the lower redshift part of the map or galaxies with redshifts too low to be viable sight lines.

In Figure 7, we show the redshift distribution of these coeval galaxies and their spatial coverage compared to the CLAMATO area. These surveys differ in their redshift accuracy: the NIR-based redshifts from MOSDEF are most accurate (Steidel et al. 2010; $\sigma_v \sim 60 \text{ km s}^{-1}$, corresponding to $\sigma_{\text{los}} \sim 0.7 h^{-1}$ Mpc), followed by the optical redshifts from VUDS, CLAMATO, and zCOSMOS (Steidel et al. 2010; Kriek et al. 2015; $\sigma_v \sim 300 \text{ km s}^{-1}$). For this analysis, we do not include galaxies from two overlapping spectroscopic surveys, 3DHST and ZFIRE. The grism redshifts from 3DHST have redshift uncertainties of $\sigma_v \gtrsim 500 \text{ km s}^{-1}$ (Kriek et al. 2015; Momcheva et al. 2016), which are comparable to the typical sizes of our voids of a few cMpc. The ZFIRE survey (Nanayakkara et al. 2016) specifically targeted the $z \sim 2.1$ protocluster (Spitler et al. 2012) and is therefore a poor choice for void validation because the galaxies will not lie in an average environment.

Galaxy positions are converted to x, y, z coordinates with the origin at $z = 2.05$, right ascension $149^{\circ}95$, and decl. $2^{\circ}15$ using the transverse comoving distance evaluated at $z = 2.3$. We convert galaxy redshift z_{gal} to coordinate position z using

$$z = (z_{\text{gal}} - 2.05) \frac{d\chi}{dz} \Big|_{z=2.3}. \quad (8)$$

Therefore, the conversion between (α, δ, z) and map coordinates (x, y, z) is identical for coeval galaxies and Ly α forest pixels.

We emphasize that this comparison is simply a validation of the cosmic void sample, and that the void-finding on the tomographic reconstruction is entirely self-sufficient. Conversely, the spectroscopic redshift galaxy samples within the field are too sparse and incomplete¹⁵ to define cosmic voids but should be sufficient to falsify a spurious detection of cosmic voids.

To compare the abundance of galaxies in voids with a control sample, we create many realizations of random catalogs with the same radius function as the void catalog. Many of the largest CLAMATO voids are preferentially located near the edge of the CLAMATO volume. Therefore, in order to reproduce the correct volume fraction in the random catalogs,

¹⁴ We use their 2016 August data release; <http://mosdef.astro.berkeley.edu/for-scientists/data-releases/>.

¹⁵ We find $n_g \sim 1.1 \times 10^{-3} h^3 \text{ Mpc}^{-3}$ for VUDS, CLAMATO, and zCOSMOS redshifts combined, compared to $n_g \sim 5 \times 10^{-3} h^3 \text{ Mpc}^{-3}$ in the VIPERS survey, which detected $z \sim 1$ voids.

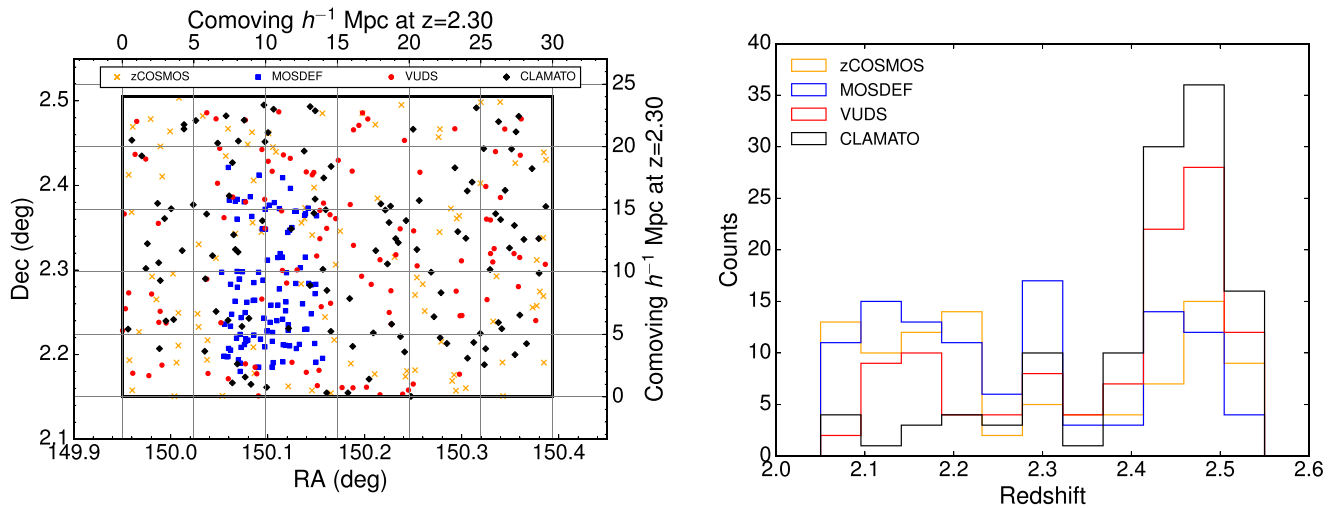


Figure 7. Left: positions of galaxies in the COSMOS field with known spectroscopic redshifts that are coeval with the $2.05 < z < 2.55$ CLAMATO map. The black box indicates the footprint of the CLAMATO map. Right: redshift distribution of coeval galaxies.

Table 3
Significances of Galaxy Underdensities in Voids

Galaxy Survey	N_{gal}	Galaxies in Voids	Galaxies in Randoms (mean)	Galaxies in Randoms (σ)	Significance
VUDS	110	13	20.36	4.29	0.0491
MOSDEF	109	6	18.49	5.45	0.0047
CLAMATO	118	10	22.07	4.67	0.0033
zCOSMOS	95	8	18.63	4.12	0.0035

Note. Significance of galaxy underdensities in four coeval galaxy surveys. CLAMATO uses the galaxies spectroscopically confirmed by our data that lie within the map volume.

we require each random cell to have the same distance from the boundary as the corresponding void with the same radius.

In detail, for each void in the catalog, we create a random cell with the same radius. If the void is located in a “corner” of the volume (i.e., the distance between both its x and y positions and the box edge is smaller than the void radius), we assign the random’s xy position by rotating the void’s xy position about the origin by either 0° , 90° , 180° , or 270° . We then randomly assign the z position. For voids not located in a corner, we randomly assign the position along the faces of a rectangular prism with distance to the CLAMATO volume edge equal to the minimum distance between the void center and the box edge. Just like the voids, the random cells are required to be nonoverlapping. We find that the random cells fill 18.9% of the CLAMATO volume (on average), compared to 19.5% of the CLAMATO volume filled by voids. As a sanity check that the random cells are indeed unbiased regions, we also find in the random cells an average absorption of $\langle \delta_F^{\text{rec}} \rangle = -6.57 \times 10^{-3} \pm 5.1 \times 10^{-3}$ (1σ standard deviation) compared to $\langle \delta_F^{\text{rec}} \rangle = -7.23 \times 10^{-3}$ for the entire map. In other words, they are both consistent with zero, as would be expected by definition (Equation (1)).

For MOSDEF, we use separate random catalogs covering the smaller area probed by this survey (Figure 7) rather than the entire CLAMATO volume. This allows the random catalogs to accurately reproduce the void fraction within the MOSDEF survey region. We use an area that extends $3 h^{-1}$ Mpc beyond the approximate MOSDEF footprint: in this case, $150^\circ 001 > \text{R.A.} > 150^\circ 203$ and $2^\circ 150 > \text{decl.} > 2^\circ 444$. We include voids that are slightly outside the MOSDEF footprint because these voids may still overlap with MOSDEF galaxies; we choose a

$3 h^{-1}$ Mpc buffer because the average void size is about $3 h^{-1}$ Mpc. The random cells fill 12.5% of the MOSDEF region volume, compared to a 12.6% void fraction in this region, with average $\delta_F^{\text{rec}} = -0.0113 \pm 0.0091$. The smaller void fraction may be due to the fact that the MOSDEF region is slightly overdense, with $\langle \delta_F^{\text{rec}} \rangle = -0.0121 \pm 0.0002$ (standard error of the mean) compared to $\langle \delta_F^{\text{rec}} \rangle = -0.0073 \pm 0.0001$ in the entire map.

The significance of the galaxy underdensity in tomographic voids is the probability that the number of galaxies in random cells is less than or equal to the number of galaxies in voids. We calculate this probability by counting the number of realizations of the random catalog with fewer galaxies in the randoms than in the tomographic voids, giving a p value for each galaxy survey. Assuming that the constraints from the different galaxy surveys are independent, the combined constraint is simply the product of the p values for the individual surveys. The distribution of galaxy counts in random cells is neither Gaussian nor Poissonian, particularly as it approaches zero galaxies where the data lies; therefore, calculating p values by direct simulation is essential, and we emphasize that the conversion to σ is purely for illustrative purposes. The errors on p values computed this way are given by $\sqrt{p(1-p)/N}$. In order to achieve $<10\%$ errors on p values, we use 10,000 realizations of the random catalog for VUDS and 300,000 realizations for CLAMATO, MOSDEF, and zCOSMOS.

We report significances in Table 3 and compare the number of galaxies in voids to the number of galaxies in random cells in Figure 8. Assuming that the galaxy surveys are independent, we find a combined p value of 3×10^{-9} , equivalent to a 5.95σ

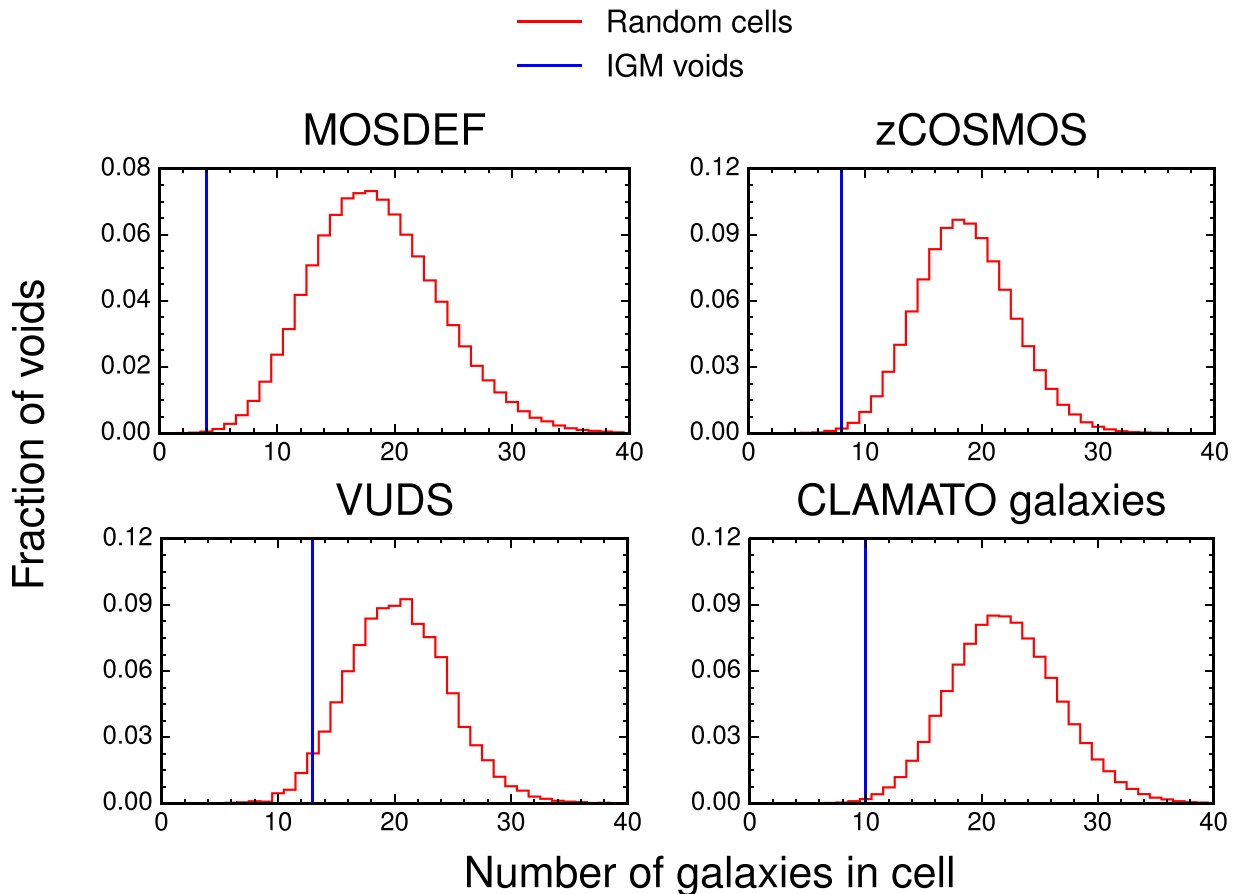


Figure 8. Distribution of the number of galaxies in random cells (red lines) compared to the number of galaxies in IGM voids (blue lines) for four galaxy surveys. The p value is the fraction of the red histogram to the left of the blue line.

detection of galaxy underdensities in the tomography-identified voids.

The significance of the galaxy underdensity in the tomographically identified voids is similar for all four surveys, although modestly lower for VUDS. These galaxies are the faintest of the surveys used ($\langle r \rangle = 24.9$, compared to $\langle r \rangle = 24.1$ for CLAMATO and zCOSMOS and $\langle r \rangle = 24.8$ for the primarily quiescent MOSDEF sample) and are thus likely to have lower bias, causing them to cluster toward voids (Conroy et al. 2005).

6. Void Properties

6.1. Void Radius Function

We compare the void radius function in CLAMATO to the void radius function in mock observations and the real-space density field (Figure 9). Due to edge effects, voids are significantly more likely to be found near the map boundaries of both the CLAMATO data and the 64 subvolumes of the N -body box with roughly CLAMATO-like geometry. As a result, we omit voids found within one void radius of the box edge. To compute the void radius function, we weight each void by the effective volume over which it could have been observed: for a void of radius r , this volume is $(30 - 2r)(24 - 2r)438 h^{-3} \text{Mpc}^3$. Omitting voids near the box edge leads to substantially better agreement with the void radius function in both the density field and the full-volume reconstruction. We also overplot the range of void radius functions found in the 64 subvolumes to give an estimate of the impact of sample

variance on this measurement; we do not plot the range for large voids where the Poisson errors become large due to the relatively small volume of both the CLAMATO and simulated survey volumes.

We compare the measured void radius function to predictions from excursion set theory (Sheth & van de Weygaert 2004; Jennings et al. 2013). The excursion set model associates voids with spherical regions that have just undergone shell crossing and have thus attained an average density of $0.2\bar{\rho}$. The evolution of voids is modeled as a random walk with two barriers, a lower barrier at $\delta_v = -2.71$, the linear underdensity of shell-crossed voids, and an upper barrier, δ_c , modeling voids squeezed out of existence by surrounding overdensities, ranging between 1.06 and 1.69. We fit two excursion set models to the data, the number-density-preserving model of Sheth & van de Weygaert (2004; SvdW) and the volume-preserving model of Jennings et al. (2013; Vdn). In both cases, $\delta_v = -2.71$ provides a poor fit, so we allow the void threshold to vary as a free parameter, finding $\delta_v = -1.44$ (-1.04) for the SvdW (Vdn) models. We use χ^2 minimization to determine the best-fit δ_v , with error bars given by the Poisson errors on the number of voids in each bin divided by the effective volume of that bin, i.e., $(30 - 2r)(24 - 2r)438 h^{-3} \text{Mpc}^3$ for a bin at radius r . Owing to the large range in n ($\geq r$), we minimize χ^2 in log space rather than linear space. We find that neither model can adequately explain the void radius function at small r ($< 3 h^{-1} \text{Mpc}$), where the error bars are substantially smaller than at large r . As a result, the best-fit curves for both models are “tilted” relative to the data at

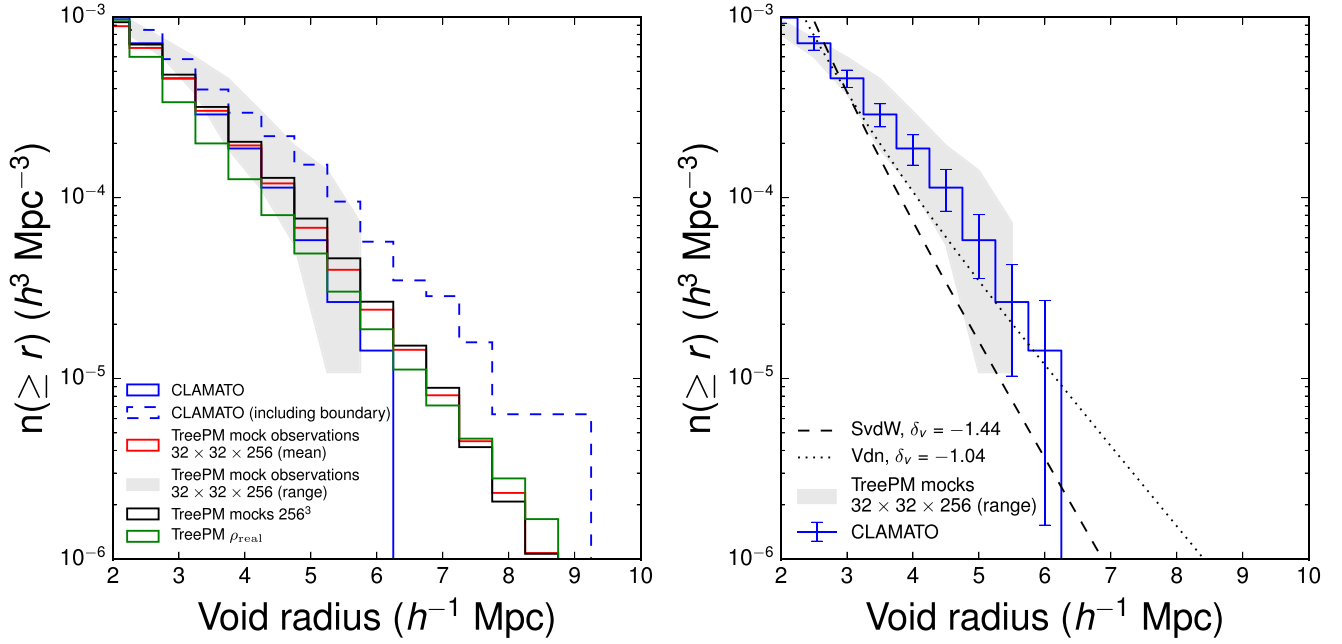


Figure 9. Left: comparison of void radius function in CLAMATO to void radius function from the N -body real-space density field, the mean and range of the void radius function from mock observations constructed from 64 $(32 \times 32 \times 256) h^{-3} \text{Mpc}^3$ subvolumes of the N -body box, and the void radius function from a mock observation constructed from the full $256^3 h^{-3} \text{Mpc}^3$ box. In all cases, we exclude voids with a distance to the boundary smaller than the void radius, except for the blue dashed line, which gives the abundance of all CLAMATO voids and thus shows the impact of edge effects on the CLAMATO void abundance. In all cases, we have centered each histogram bin over the corresponding void radius: i.e., the bin centered at $3 h^{-1} \text{Mpc}$ gives the number of voids with radius greater than or equal to $3 h^{-1} \text{Mpc}$. Right: comparison of the CLAMATO void radius function to excursion set models (black lines), with the range of the 64 N -body subvolumes overlotted to give a sense of the error on the measured void radius function. Error bars on the data are Poisson error bars on the counts in each bin, divided by the effective volume of that bin.

$r \geq 3 h^{-1} \text{Mpc}$ due to the smaller error bars and thus larger impact of the points at small r . While neither model can fit the void radius function at small radii, the Vdn model adequately fits the data at large r and provides a notably better fit than the SvdW model.

We expect a higher value of δ_v than -2.71 for the void radius function in our work because we use a higher mean overdensity of voids ($\bar{\rho} = 0.4$); indeed, our results are similar to the results of Jennings et al. (2013), who found $\delta_v = -1.24$ for $\bar{\rho} = 0.4$. Our results also lie in the same general range as previous results, which find δ_v between -0.2 and -1.0 (Sutter et al. 2014b; Nadathur & Hotchkiss 2015; Pisani et al. 2015). However, Jennings et al. (2013), working between $z = 0$ and 1, recommended models with a considerably smaller void abundance than found here (1/5 the abundance of the Sheth & van de Weygaert 2004 prediction with $\delta_v = -1.24$, about five times lower than our data).

6.2. Radial Void Profile

We plot radially averaged void profiles in Figure 10 for all voids with $r \geq 5 h^{-1} \text{Mpc}$, normalizing each void to its void radius and stacking in units of the void radius r/r_v . There is good agreement between void profiles in data and mock observations, with $\chi^2 = 22.1$ over 16 radial bins between the void profile in CLAMATO and the void profile in mock observations from the N -body simulations. Since each bin is $0.1 r_v \sim 0.5 h^{-1} \text{Mpc}$, much smaller than $\langle d_{\perp} \rangle = 2.5 h^{-1} \text{Mpc}$, the void profile is highly correlated between neighboring bins, so we cannot assume a diagonal covariance matrix when computing χ^2 (i.e., the χ^2 quoted above uses the full covariance matrix and is much lower than if this covariance matrix were diagonal). We compute the covariance matrix

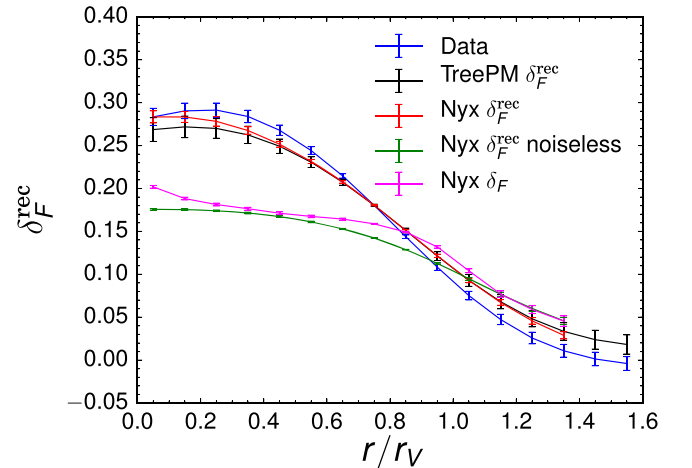


Figure 10. Radially averaged void profiles in data (blue), mock observations (black for N -body box and red for hydrodynamic box), noiseless mock observations (green), and underlying δ_F (magenta), stacked in units of the void radius r_v for all voids with $r \geq 5 h^{-1} \text{Mpc}$. Error bars for the Nyx profile are estimated using 1000 realizations of the void catalog generated via bootstrap resampling, while error bars for the TreePM and data profiles are generated from the standard deviation over the 64 subvolumes of the TreePM box.

using the 64 subvolumes of the N -body box and scale down the covariance by 0.8, the volume ratio between the N -body subvolumes and the CLAMATO volume. We also use the unbiased estimator of Hartlap et al. (2007) for the inverse covariance matrix for the case where the mean is estimated from the data (their Equation (17)). The strong agreement between the radial void profile in mock observations and data suggests that approximations in the map-making process (e.g.,

the distance-redshift and angle-redshift conversion discussed in Section 2) make only a minor impact on the void profile.

The void profile in mock observations traces the void profile in the underlying Ly α flux field, δ_F , well for $r > r_V$ but deviates badly inside the void. This deviation is due almost entirely to noise in the spectra, with the profiles in noiseless reconstructions resembling the δ_F profiles much more closely. Unfortunately, the deviation between void profiles in δ_F^{rec} and δ_F means that void profiles in the reconstruction do not trace void profiles in matter, and thus we do not try to fit a functional form to the void profile (e.g., Ceccarelli et al. 2006; Hamaus et al. 2014; White & Padmanabhan 2017), as it could not be compared with low-redshift results.

Qualitatively, the void profile in the data is missing the “compensation wall” that is present in some low-redshift void profiles, particularly voids with $r < 20 h^{-1}$ Mpc like those discussed here (Hamaus et al. 2014). It is unclear whether the absence of a compensation wall is indicative of physical differences between high- and low-redshift voids or is merely an artifact of our void finder and void sample. For instance, while our voids are small at $z \sim 2.3$, they will become much bigger by $z \sim 0$; Sheth & van de Weygaert (2004) found $r_V \propto (1+z)^{-2/(3+n)}$, where $n \sim -1.5$ is the slope of the power spectrum on scales of the void size. Therefore, $5 h^{-1}$ Mpc voids at $z = 2.3$ correspond to $25 h^{-1}$ Mpc voids at $z = 0$, which generally have a very weak or absent compensation wall (Cai et al. 2015; Hamaus et al. 2016). On the other hand, White & Padmanabhan (2017) suggested that spherical overdensity finders may not find compensation walls, while Cai et al. (2016) argued that compensation walls are only present in voids found in overdense environments.

We also study the impact of redshift-space distortions on $z \sim 2$ voids. Redshift-space distortions modify the void profile along the line of sight and are often measured using the quadrupole of a correlation function or void profile. Numerical simulations find that for $r \gtrsim r_V$ in uncompensated voids, isodensity contours are flattened along the line of sight in the same sense as the Kaiser (1987) effect for overdensities (Cai et al. 2016; Nadathur & Percival 2017). On smaller scales, nonlinear effects such as velocity dispersion may lead to extended profiles along the line of sight (Cai et al. 2016), although the magnitude of these effects is unclear (see discussion in Nadathur & Percival 2017). We replicate these findings for simulated voids at $z \sim 2$ in the underlying flux and density fields for the entire $256^3 h^{-3} \text{Mpc}^3$ box.

However, we find that when measured in $(32 \times 32 \times 256) h^{-3} \text{Mpc}^3$ CLAMATO-like subvolumes, the void quadrupole is significantly distorted by edge effects in the Wiener filter and void finder. We also find that the void quadrupole is significantly distorted by continuum error, since continuum error is correlated along the line of sight. Due to the large impact of these systematic effects, we do not present redshift-space distortion measurements in CLAMATO voids here. Future surveys with a larger contiguous area (e.g., an IGM tomography survey on the Subaru Prime Focus Spectrograph (PFS) over 20 deg^2) will be less impacted by continuum errors; we find very good agreement between the void quadrupole in a $128 \times 128 \times 256 h^{-3} \text{Mpc}^3$ subvolume and the full TreePM box. However, continuum error will remain a major source of systematic error for modeling redshift-space distortions in Ly α forest voids: either the effects of continuum error must be removed, e.g., by ignoring correlated pixels along the line of sight, or we require

accurate end-to-end modeling of the effects of continuum error on void shapes.

7. Conclusions

We present the first detection of cosmic voids at $z \sim 2$ using a spherical overdensity finder applied to a tomographic map of the 3D Ly α absorption field from the CLAMATO survey carried out on the Keck I telescope. By targeting background Lyman break galaxy (LBG) and quasar sight lines with mean transverse separation $2.5 h^{-1}$ Mpc at $z \sim 2.3$, we create a Wiener-filtered map of the neutral hydrogen density on few Mpc scales, which is an excellent tracer of the underlying matter density. This allows us to measure the density field on scales considerably smaller than current galaxy surveys can achieve at this redshift, enabling cosmic void detection at far greater ($\sim 1.7\times$) cosmic distance than the hitherto most distant cosmic voids at $z \sim 1$.

Building on the results of Stark et al. (2015a), we use realistic mock observations based on hydrodynamical and N -body simulations to calibrate thresholds for identifying voids in IGM maps. This is necessary to better model the Ly α forest and continuum errors in the survey, which were neglected in Stark et al. (2015a). Within the simulations, we find worse void recovery from IGM tomography than Stark et al. (2015a): $\sim 40\%$ of tomographically identified voids are well matched to density field voids for $r \geq 5 h^{-1}$ Mpc.

Using thresholds calibrated from simulations, we apply the void finder to the CLAMATO map to find a 19.5% volume fraction of voids. After removing voids affected by edge effects, we find good agreement between the void radius function in simulations and data. Excursion set models can fit the void radius function only if the excursion set threshold is adjusted considerably from the Sheth & van de Weygaert (2004) prediction of -2.71 .

We also study the stacked void profiles for the higher-confidence subsample of large ($r \geq 5 h^{-1}$ Mpc) voids. As in Stark et al. (2015a), we find no compensation ridge in the radial void profiles, consistent with other spherical overdensity finders (White & Padmanabhan 2017).

We validate the void detection by finding that these voids are $\sim 6\sigma$ underdense in coeval galaxies from the MOSDEF, VUDS, and zCOSMOS spectroscopic redshift surveys, as well as CLAMATO-confirmed galaxies falling within the tomographic volume. While the galaxy catalogs are unable to detect voids on their own, they validate the detection of voids in IGM tomography by showing that our voids have significantly fewer galaxies than random regions with the same radius distribution.

Identifying cosmic voids requires both a large volume and a reasonably dense sampling of the density field. Previous detections of voids from galaxy surveys have extended to $z \sim 1$ (Conroy et al. 2005; Ceccarelli et al. 2006; Sutter et al. 2012; Micheletti et al. 2014; Mao et al. 2017b; Sánchez et al. 2017), while IGM tomography can detect voids at $z \sim 2.3$, providing by far the most distant sample of voids owing to much denser sampling of the density field than galaxy surveys at comparable redshifts. Moreover, upcoming surveys will dramatically increase the number of $z \sim 2.5$ voids detected via IGM tomography. We find 48 voids with $r \geq 5 h^{-1}$ Mpc (for which we expect $\geq 45\%$ void recovery); the full CLAMATO survey will cover ~ 3 – 5 times more volume than

the data used in this paper, and thus we expect to find $>100r \geq 5 h^{-1}$ Mpc voids, in line with the estimates in Stark et al. (2015a). Moreover, PFS on the Subaru telescope will begin operation by 2020 (Takada et al. 2014); it will allow for surveys covering a much wider area, owing to the much larger field of view of PFS compared to LRIS. A dedicated IGM tomography survey building on the PFS galaxy evolution survey could cover $15\text{--}20 \text{ deg}^2$ with sight-line separation $3\text{--}4 h^{-1}$ Mpc, i.e., comparable or slightly worse sampling than CLAMATO; the exact parameters are currently under discussion within the PFS collaboration. Thus, such a survey on PFS could find 2000 $z \sim 2.5$ voids (Stark et al. 2015a) with comparable fidelity to CLAMATO. The larger area could be particularly crucial to detecting void redshift-space distortions at high significance.

At low redshifts, voids have been used for Alcock–Paczynski tests to measure cosmological parameters, since voids are, on average, spherical in real space (Sutter et al. 2014c; Mao et al. 2017a). Stark et al. (2015a) estimated that a competitive high-redshift measurement of the Alcock–Paczynski parameter will require 10,000 voids, which could be achieved by a dedicated 100 night tomography survey on PFS or shorter surveys on even more ambitious instruments, such as the Maunakea Spectroscopic Explorer (McConnachie et al. 2016) or the Billion Object Apparatus (Dodelson et al. 2016). On the other hand, Stark et al. (2015a) found that linear theory accurately predicts the radial velocity profile of voids, suggesting that studying the velocity field either to infer cosmological parameters (e.g., Hamaus et al. 2016, using redshift-space distortions at low redshift) or to test modified gravity theories could be promising avenues of exploration. In particular, Clampitt et al. (2013) estimated that modified gravity theories could alter void profiles in a way that could be observed with samples of 20 voids.

Finally, voids offer an intriguing test bed for galaxy formation, as they contain halos that have grown primarily by diffuse accretion rather than mergers (Fakhouri & Ma 2009). Existing studies of galaxy formation in voids have been limited to low redshift, where differences in void galaxy properties can be attributed largely to their different stellar masses (Hoyle et al. 2005; Tinker et al. 2008; Alpaslan et al. 2015; Penny et al. 2015; Beygu et al. 2016). However, this may be different at high redshift, particularly since the global star formation rate at $z \sim 2$ is much higher than that at $z \sim 0$. In principle, we have already identified 35 galaxies in voids; however, if a tomography-identified void contains a galaxy, it is more likely that it is a fluctuation due to noise than otherwise. Stark et al. (2015a) pointed out that “true” voids are expected to be devoid of such bright galaxies, but voids could contain faint $L \sim 0.3 L_*$ galaxies that could be observed by the NIRSPEC spectrograph on *JWST*.










We thank Shirley Ho, Uroš Seljak, Joanne Cohn, and Zachary Slepian for helpful comments on this work. K.G.L. acknowledges support for this work by NASA through Hubble Fellowship grant HF2-51361, awarded by the Space Telescope Science Institute, which is operated by the Association of Universities for Research in Astronomy, Inc., for NASA, under contract NAS5-26555. We are also grateful to the entire COSMOS collaboration for their assistance and helpful discussions. Calculations presented in this paper used resources of the National Energy Research Scientific Computing Center

(NERSC), which is supported by the Office of Science of the U.S. Department of Energy under contract No. DE-AC02-05CH11231. The data presented herein were obtained at the W.M. Keck Observatory, which is operated as a scientific partnership among the California Institute of Technology, the University of California, and the National Aeronautics and Space Administration (NASA). The observatory was made possible by the generous financial support of the W.M. Keck Foundation. The authors thank Yong’s Kal-Bi in Waimea, HI, for vital sustenance during our observations. The authors also wish to recognize and acknowledge the very significant cultural role and reverence that the summit of Maunakea has always had within the indigenous Hawai’ian community. We are most fortunate to have the opportunity to conduct observations from this mountain.

Appendix

We have made the CLAMATO void catalog (Table 2) publicly available at doi:[10.5281/zenodo.1295839](https://doi.org/10.5281/zenodo.1295839). We have also included void catalogs from the mock CLAMATO-like observations in the Nyx and TreePM box, including void catalogs from both the full TreePM box and the 64 subvolumes and void catalogs from the (real- and redshift-space) density fields and underlying flux of the Nyx simulation, corresponding to the void fractions reported in Table 1. We have also included the mock CLAMATO maps from these simulations.

ORCID iDs

Alex Krolewski  <https://orcid.org/0000-0003-2183-7021>
 Khee-Gan Lee  <https://orcid.org/0000-0001-9299-5719>
 Martin White  <https://orcid.org/0000-0001-9912-5070>
 Joseph F. Hennawi  <https://orcid.org/0000-0002-7054-4332>
 David J. Schlegel  <https://orcid.org/0000-0002-5042-5088>
 Peter E. Nugent  <https://orcid.org/0000-0002-3389-0586>
 Casey W. Stark  <https://orcid.org/0000-0002-1252-3250>
 Anton M. Koekemoer  <https://orcid.org/0000-0002-6610-2048>
 Christian Maier  <https://orcid.org/0000-0001-6405-2182>
 Mara Salvato  <https://orcid.org/0000-0001-7116-9303>

References

- Alcock, C., & Paczynski, B. 1979, *Natur*, 281, 358
 Almgren, A. S., Bell, J. B., Lijewski, M. J., Lukić, Z., & Van Andel, E. 2013, *ApJ*, 765, 39
 Alpaslan, M., Driver, S., Robotham, A. S. G., et al. 2015, *MNRAS*, 451, 3249
 Banerjee, A., & Dalal, N. 2016, *JCAP*, 11, 015
 Barreira, A., Cautun, M., Li, B., Baugh, C. M., & Pascoli, S. 2015, *JCAP*, 8, 028
 Beygu, B., Kreckel, K., van der Hulst, J. M., et al. 2016, *MNRAS*, 458, 394
 Beygu, B., Peletier, R. F., van der Hulst, J. M., et al. 2017, *MNRAS*, 464, 666
 Bolton, J. S., Puchwein, E., Sijacki, D., et al. 2017, *MNRAS*, 464, 897
 Bolton, J. S., Viel, M., Kim, T.-S., Haehnelt, M. G., & Carswell, R. F. 2008, *MNRAS*, 386, 1131
 Bond, J. R., Kofman, L., & Pogosyan, D. 1996, *Natur*, 380, 603
 Bos, E. G. P., van de Weygaert, R., Dolag, K., & Pettorino, V. 2012, *MNRAS*, 426, 440
 Cai, Y.-C., Neyrinck, M., Mao, Q., et al. 2017, *MNRAS*, 466, 3364
 Cai, Y.-C., Padilla, N., & Li, B. 2015, *MNRAS*, 451, 1036
 Cai, Y.-C., Taylor, A., Peacock, J. A., & Padilla, N. 2016, *MNRAS*, 462, 2465
 Cauci, S., Colombi, S., Pichon, C., et al. 2008, *MNRAS*, 386, 211
 Ceccarelli, L., Padilla, N. D., Valotto, C., & Lambas, D. G. 2006, *MNRAS*, 373, 1440
 Clampitt, J., Cai, Y.-C., & Li, B. 2013, *MNRAS*, 431, 749
 Clampitt, J., & Jain, B. 2015, *MNRAS*, 454, 3357

- Conroy, C., Coil, A. L., White, M., et al. 2005, *ApJ*, 635, 990
- Dodelson, S., Heitmann, K., Hirata, C., et al. 2016, arXiv:1604.07626
- Doran, M., & Robbers, G. 2006, *JCAP*, 6, 026
- Fakhouri, O., & Ma, C.-P. 2009, *MNRAS*, 394, 1825
- Faucher-Giguère, C.-A., Prochaska, J. X., Lidz, A., Hernquist, L., & Zaldarriaga, M. 2008, *ApJ*, 681, 831
- Goldberg, D. M., & Vogeley, M. S. 2004, *ApJ*, 605, 1
- Granett, B. R., Neyrinck, M. C., & Szapudi, I. 2008, *ApJL*, 683, L99
- Gruen, D., Friedrich, O., Amara, A., et al. 2016, *MNRAS*, 455, 3367
- Haardt, F., & Madau, P. 1996, *ApJ*, 461, 20
- Hamaus, N., Cousinou, M.-C., Pisani, A., et al. 2017, *JCAP*, 7, 014
- Hamaus, N., Pisani, A., Sutter, P. M., et al. 2016, *PhRvL*, 117, 091302
- Hamaus, N., Sutter, P. M., & Wandelt, B. D. 2014, *PhRvL*, 112, 251302
- Hartlap, J., Simon, P., & Schneider, P. 2007, *A&A*, 464, 399
- Higuchi, Y., Oguri, M., & Hamana, T. 2013, *MNRAS*, 432, 1021
- Hoyle, F., Rojas, R. R., Vogeley, M. S., & Brinkmann, J. 2005, *ApJ*, 620, 618
- Jennings, E., Li, Y., & Hu, W. 2013, *MNRAS*, 434, 2167
- Kaiser, N. 1987, *MNRAS*, 227, 1
- Kovács, A., Sánchez, C., García-Bellido, J., et al. 2017, *MNRAS*, 465, 4166
- Krause, E., Chang, T.-C., Doré, O., & Umetsu, K. 2013, *ApJL*, 762, L20
- Krekel, K., Platen, E., Aragón-Calvo, M. A., et al. 2012, *AJ*, 144, 16
- Kriek, M., Shapley, A. E., Reddy, N. A., et al. 2015, *ApJS*, 218, 15
- Krolewski, A., Lee, K.-G., Lukić, Z., & White, M. 2017, *ApJ*, 837, 31
- Lam, T. Y., Clampitt, J., Cai, Y.-C., & Li, B. 2015, *MNRAS*, 450, 3319
- Lavaux, G., & Wandelt, B. D. 2012, *ApJ*, 754, 109
- Le Fèvre, O., Tasca, L. A. M., Cassata, P., et al. 2015, *A&A*, 576, A79
- Lee, J., & Park, D. 2009, *ApJL*, 696, L10
- Lee, K.-G. 2012, *ApJ*, 753, 136
- Lee, K.-G., Bailey, S., Bartsch, L. E., et al. 2013, *AJ*, 145, 69
- Lee, K.-G., Hennawi, J. F., Spergel, D. N., et al. 2015, *ApJ*, 799, 196
- Lee, K.-G., Hennawi, J. F., White, M., Croft, R. A. C., & Ozbek, M. 2014, *ApJ*, 788, 49
- Lee, K.-G., Krolewski, A., White, M., et al. 2017, arXiv:1710.02894
- Lee, K.-G., Suzuki, N., & Spergel, D. N. 2012, *AJ*, 143, 51
- Lee, K.-G., & White, M. 2016, *ApJ*, 831, 181
- Li, B., Zhao, G.-B., & Koyama, K. 2012, *MNRAS*, 421, 3481
- Lilly, S. J., Le Fèvre, O., Renzini, A., et al. 2007, *ApJs*, 172, 70
- Lukić, Z., Stark, C. W., Nugent, P., et al. 2015, *MNRAS*, 446, 3697
- Mao, Q., Berlind, A. A., Scherrer, R. J., et al. 2017a, *ApJ*, 835, 160
- Mao, Q., Berlind, A. A., Scherrer, R. J., et al. 2017b, *ApJ*, 835, 161
- Massara, E., Villaescusa-Navarro, F., Viel, M., & Sutter, P. M. 2015, *JCAP*, 11, 018
- McConnachie, A., Babusiaux, C., Balogh, M., et al. 2016, arXiv:1606.00043
- Melchior, P., Sutter, P. M., Sheldon, E. S., Krause, E., & Wandelt, B. D. 2014, *MNRAS*, 440, 2922
- Micheletti, D., Iovino, A., Hawken, A. J., et al. 2014, *A&A*, 570, A106
- Momcheva, I. G., Brammer, G. B., van Dokkum, P. G., et al. 2016, *ApJs*, 225, 27
- Nadathur, S., & Hotchkiss, S. 2015, *MNRAS*, 454, 2228
- Nadathur, S., & Percival, W. J. 2017, arXiv:1712.07575
- Nanayakkara, T., Glazebrook, K., Kacprzak, G. G., et al. 2016, *ApJ*, 828, 21
- Neyrinck, M. C. 2008, *MNRAS*, 386, 2101
- Oke, J. B., Cohen, J. G., Carr, M., et al. 1995, *PASP*, 107, 375
- Pan, D. C., Vogeley, M. S., Hoyle, F., Choi, Y.-Y., & Park, C. 2012, *MNRAS*, 421, 926
- Park, D., & Lee, J. 2007, *PhRvL*, 98, 081301
- Peebles, P. J. E. 2001, *ApJ*, 557, 495
- Penny, S. J., Brown, M. J. I., Pimblet, K. A., et al. 2015, *MNRAS*, 453, 3519
- Pichon, C., Vergely, J. L., Rollinde, E., Colombi, S., & Petitjean, P. 2001, *MNRAS*, 326, 597
- Pisani, A., Sutter, P. M., Hamaus, N., et al. 2015, *PhRvD*, 92, 083531
- Planck Collaboration, Adam, R., Ade, P. A. R., et al. 2016, *A&A*, 594, A1
- Pollina, G., Baldi, M., Marulli, F., & Moscardini, L. 2016, *MNRAS*, 455, 3075
- Rollinde, E., Petitjean, P., Pichon, C., et al. 2003, *MNRAS*, 341, 1279
- Rorai, A., Becker, G. D., Haehnelt, M. G., et al. 2017, *MNRAS*, 466, 2690
- Ryden, B. S. 1995, *ApJ*, 452, 25
- Sánchez, C., Clampitt, J., Kovacs, A., et al. 2017, *MNRAS*, 465, 746
- Sheth, R. K., & van de Weygaert, R. 2004, *MNRAS*, 350, 517
- Spitler, L. R., Labbé, I., Glazebrook, K., et al. 2012, *ApJL*, 748, L21
- Stark, C. W., Font-Ribera, A., White, M., & Lee, K.-G. 2015a, *MNRAS*, 453, 4311
- Stark, C. W., White, M., Lee, K.-G., & Hennawi, J. F. 2015b, *MNRAS*, 453, 311
- Steidel, C. C., Erb, D. K., Shapley, A. E., et al. 2010, *ApJ*, 717, 289
- Steidel, C. C., Shapley, A. E., Pettini, M., et al. 2004, *ApJ*, 604, 534
- Sutter, P. M., Lavaux, G., Hamaus, N., et al. 2014a, *MNRAS*, 442, 462
- Sutter, P. M., Lavaux, G., Wandelt, B. D., et al. 2014b, *MNRAS*, 442, 3127
- Sutter, P. M., Lavaux, G., Wandelt, B. D., & Weinberg, D. H. 2012, *ApJ*, 761, 44
- Sutter, P. M., Pisani, A., Wandelt, B. D., & Weinberg, D. H. 2014c, *MNRAS*, 443, 2983
- Takada, M., Ellis, R. S., Chiba, M., et al. 2014, *PASJ*, 66, R1
- Tejos, N., Morris, S. L., Crighton, N. H. M., et al. 2012, *MNRAS*, 425, 245
- Tinker, J. L., & Conroy, C. 2009, *ApJ*, 691, 633
- Tinker, J. L., Conroy, C., Norberg, P., et al. 2008, *ApJ*, 686, 53
- van de Weygaert, R., & Platen, E. 2011, *IJMPS*, 1, 41
- Viel, M., Colberg, J. M., & Kim, T.-S. 2008, *MNRAS*, 386, 1285
- Viel, M., Schaye, J., & Booth, C. M. 2013, *MNRAS*, 429, 1734
- Villaescusa-Navarro, F., Vogelsberger, M., Viel, M., & Loeb, A. 2013, *MNRAS*, 431, 3670
- White, M. 2002, *ApJS*, 143, 241
- White, M., & Padmanabhan, N. 2017, *MNRAS*, 471, 1167
- White, M., Pope, A., Carlson, J., et al. 2010, *ApJ*, 713, 383
- Zivick, P., Sutter, P. M., Wandelt, B. D., Li, B., & Lam, T. Y. 2015, *MNRAS*, 451, 4215